



# Evidence for crustal low shear-wave speed in western Saudi Arabia from multi-scale fundamental-mode Rayleigh-wave group-velocity tomography

Zheng Tang<sup>a,\*</sup>, P. Martin Mai<sup>a</sup>, Sung-Joon Chang<sup>b</sup>, Hani Zahran<sup>c</sup>

<sup>a</sup> King Abdullah University of Science and Technology (KAUST), Thuwal, Saudi Arabia

<sup>b</sup> Kangwon National University (KNU), Chuncheon, South Korea

<sup>c</sup> Saudi Geological Survey (SGS), Jeddah, Saudi Arabia

## ARTICLE INFO

### Article history:

Received 7 December 2017

Received in revised form 30 April 2018

Accepted 2 May 2018

Available online xxxx

Editor: P. Shearer

### Keywords:

Rayleigh-wave  
group-velocity tomography  
shear-velocity inversion  
Arabian Shield  
Cenozoic volcanism

## ABSTRACT

We investigate the crustal and upper-mantle shear-velocity structure of Saudi Arabia by fundamental-mode Rayleigh-wave group-velocity tomography and shear-wave velocity inversion. The seismic dataset is compiled using ~140 stations of the Saudi National Seismic Network (SNSN) operated by the Saudi Geological Survey (SGS). We measure Rayleigh-wave group-velocities at periods of 8–40 s from regional earthquakes. After obtaining 1-D shear-wave velocity models by inverting group-velocities at each grid node, we construct a 3-D shear-velocity model for Saudi Arabia and adjacent regions by interpolating the 1-D models. Our 3-D model indicates significant lateral variations in crustal and lithospheric thickness, as well as in the shear-wave velocity over the study region. In particular, we identify zones of reduced shear-wave speed at crustal levels beneath the Cenozoic volcanic fields in the Arabian Shield. The inferred reductions of 2–5% in shear-wave speed may be interpreted as possibly indicating the presence of partial melts. However, their precise origin we can only speculate about. Our study also reveals an upper-mantle low velocity zone (LVZ) below the Arabian Shield, supporting the model of lateral mantle flow from the Afar plume. Further geophysical experiments are needed to confirm (or refute) the hypothesis that partial melts may exist below the Cenozoic volcanism in western Saudi Arabia, and to build a comprehensive geodynamic–geological model for the evolution and present state of the lithosphere of the Arabian Plate and the Red Sea.

© 2018 Elsevier B.V. All rights reserved.

## 1. Introduction

The Arabian Plate started to separate from Africa as the Red Sea and Aden Gulf rifting began around 30 Ma ago (e.g., Camp and Roobol, 1992; Bosworth et al., 2005; Garfunkel and Beyth, 2006). It is geologically divided into two distinct terrains: the western Arabian Shield and the eastern Arabian Platform (Fig. 1). Extensive Precambrian Proterozoic basement rocks are exposed in the Arabian Shield, although they underlie the entire Arabian Peninsula. Cenozoic volcanic rocks, known as “harrats”, mainly overlie the western part of the Arabian Shield. The Arabian Platform is covered by predominant Paleozoic, Mesozoic and Cenozoic sedimentary rocks with increasing thickness eastward away from the Shield (Brown, 1972; Stoeser and Camp, 1985).

The rifting of the Red Sea strongly affected the geology and recent tectonic history of western Saudi Arabia. Some studies suggest that the Red Sea is passively rifting, driven by extensional stresses due to far-field forces such as slab pull (e.g. Wernicke, 1985; McGuire and Bohannon, 1989; Koulakov et al., 2016). Other studies (e.g. Bellahsen et al., 2003; Hansen et al., 2007) argue that the Red Sea developed as an active rift, driven by hot mantle upwelling that leads to thermal uplift and lithospheric thinning. In addition, the hypothesis of hybrid rifting has been proposed in which the Red Sea opening is thought to be initiated passively, but is then followed by a period of active processes (Camp and Roobol, 1992; Ebinger and Sleep, 1998; Daradich et al., 2003). The stage of rifting is non-uniform along the Red Sea. The southern Red Sea already indicates seafloor spreading and prominent volcanic activity (Ebinger and Sleep, 1998; Daradich et al., 2003; Xu and Jónsson, 2014), while the northern Red Sea is still at a passive rifting stage (Kaban et al., 2016), and/or an active rift at the end of its continental stage beginning to transit into oceanic seafloor spreading (Cochran and Martinez, 1988).

\* Correspondence to: P.O. Box 4700-3770, Thuwal, Jeddah, 23955-6900, Saudi Arabia.

E-mail address: Zheng.Tang@kaust.edu.sa (Z. Tang).

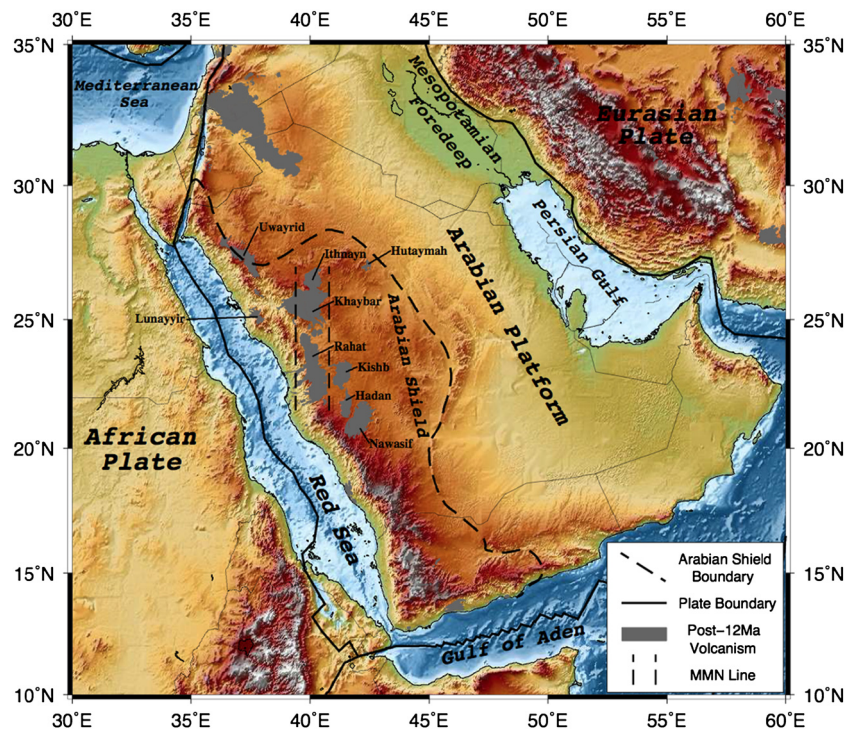


**Fig. 1.** Geographic map of the Arabian Plate and its surrounding regions, showing the main geologic features, the Cenozoic volcanism during the past 12 Ma (gray-shaded regions), and the so-called Makkah–Madinah–Nafud (MMN) volcanic line. Main volcanic regions (called harrats locally) are indicated by their names to which we refer in the text.

Western Arabia is dotted with areas of Cenozoic volcanism that formed during the past 30 Ma, showing a bimodal chemical character that indicates two distinct phases of volcanism (Camp and Roobol, 1992). Older lavas (30–20 Ma) are tholeiitic to transitional in composition. These are oriented approximately parallel to the Red Sea and have been attributed to the early rifting stage of the Red Sea. In contrast, younger lavas (12 Ma to recent) are transitional to alkalic, and can be found mainly along the north–south oriented Makkah–Madinah–Nafud (MMN) line. Chang and Van der Lee (2011) suggests that the pronounced Cenozoic volcanism originates from lateral mantle flow from the Afar and, perhaps, a hypothesized Jordan hotspot. Other studies argue that a local mantle plume (Camp and Roobol, 1992) and/or a local hot mantle upwelling (Koulakov et al., 2016) under the Arabian Plate may play a key role in the formation of the Cenozoic lava fields.

Several geophysical studies of crustal and upper-mantle structure of the Arabian Plate provide evidence for lateral variations of lithospheric properties (e.g., Mooney et al., 1985; Gettings et al., 1986; Mokhtar and Al-Saeed, 1994; Sandvol et al., 1998; Rodgers et al., 1999; Mokhtar et al., 2001; Kumar et al., 2002; Julià et al., 2003; Al-Damegh et al., 2005; Tkalčić et al., 2006; Hansen et al., 2007; Chang and Van der Lee, 2011; Tang et al., 2016; Yao et al., 2017). Generally, the crustal thickness in the Arabian Shield varies between 27 and 45 km (Hansen et al., 2007; Tang et al., 2016), while the crustal shear-velocity ranges from 3.48 to 3.95 km/s with an average bulk  $V_p/V_s$  ratio of  $1.73 \pm 0.07$  (Tang et al., 2016). Thinner crust (25–32.5 km thick) with strong lateral variations is present along the Red Sea margin (Al-Damegh et al., 2005; Tkalčić et al., 2006; Tang et al., 2016). The Arabian Platform has crustal shear-velocities between 3.44 and 3.68 km/s and an average bulk  $V_p/V_s$  of  $1.77 \pm 0.09$  (Tang et al., 2016).

In addition, it has been inferred that the depth of the lithosphere–asthenosphere boundary (LAB) varies considerably across the Arabian Peninsula, showing thin lithosphere under western Arabia that thickens toward the Arabian interior (Hansen et al., 2007). Tkalčić et al. (2006) observes anomalously low upper-

mantle velocities and strong polarization anisotropy in the lithospheric upper-mantle below the Arabian Shield. Chang and Van der Lee (2011) and Chang et al. (2011) find slow shear-wave velocities at  $\sim 150$  km depth, stretching from the Afar through the southern Red Sea and into the western Arabia, as well as a quasi-vertical low velocity anomaly under Jordan. Yao et al. (2017) confirms the upper-mantle low velocity zone (LVZ) of  $\sim 300$  km width, roughly 60–190 km depths, and trending approximately north–south below the MMN volcanic line.

However, most of the above-mentioned studies are limited by poor station coverage and sparse datasets. Thus, there is still considerable ambiguity regarding the lateral variations of crustal and upper-mantle structure below the Arabian Shield, the regions of Cenozoic volcanism (harrats), and the Arabian Platform. In this study, we aim to revise previous models by conducting a fundamental-mode Rayleigh-wave group-velocity tomography and inverting for 3-D shear-wave velocity structure underneath Saudi Arabia, based on a new seismic datasets obtained from the Saudi Geological Survey (SGS). The new observations include seismic data recorded by a dense station network (unavailable for previous studies) in the years of 2007–2014, which greatly improves the spatial coverage and helps illuminating intraplate regions. Our study therefore extends previous efforts to map crustal and upper-mantle structure of Saudi Arabia, and achieves higher local resolution.

In the following, we first describe the seismic data and our Rayleigh-wave group-velocity measurements. The next section presents the Rayleigh-wave tomography method and resulting maps of Rayleigh-wave group-velocities, followed by the description of the shear-wave velocity inversion and the estimated 3-D velocity model for the entire study region. Finally, we examine in detail the local velocity structure below the regions of Cenozoic volcanism in the Arabian Shield and discuss possible interpretations for the observed spatial patterns of shear-wave velocity variations.

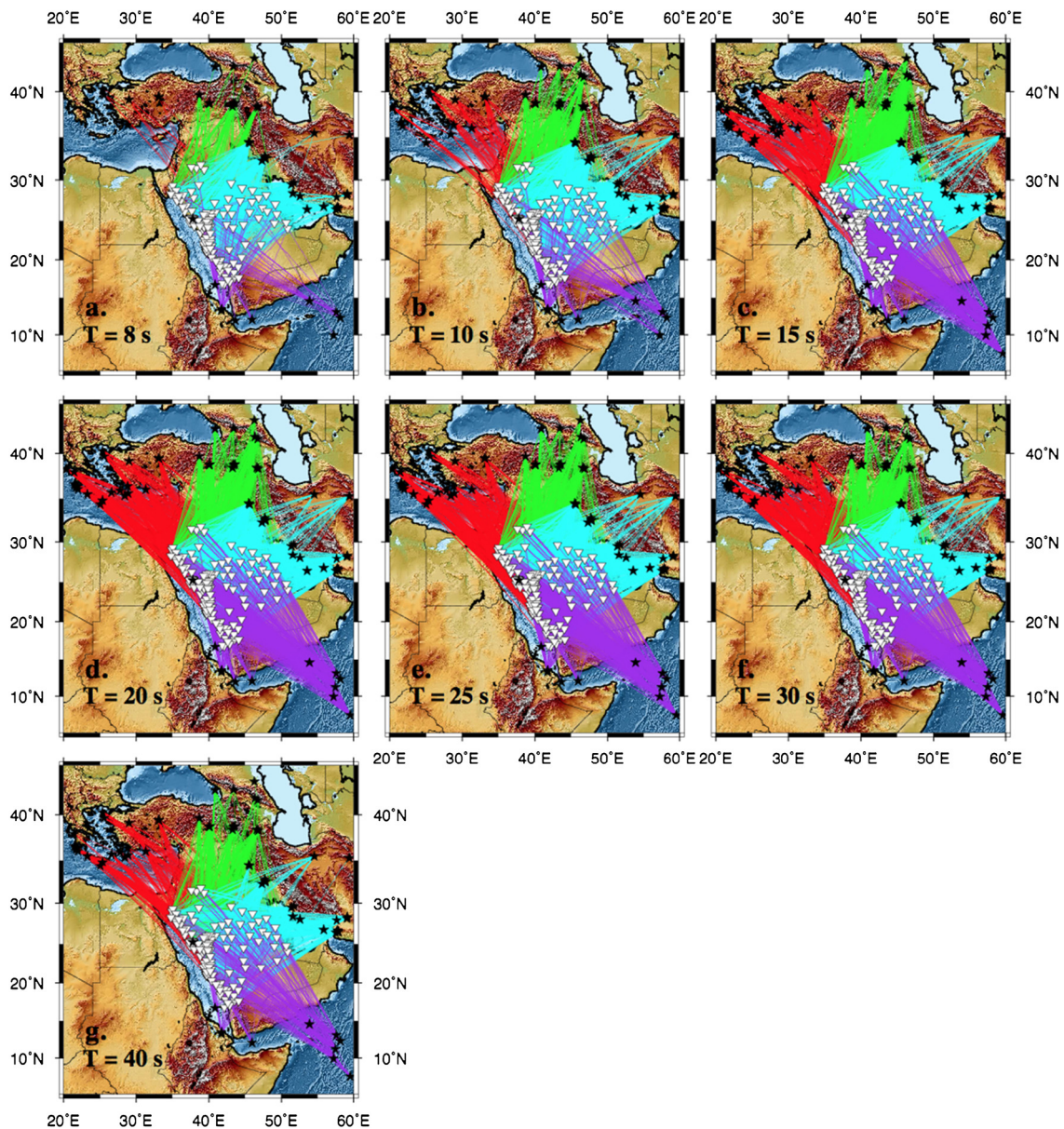


**Fig. 2.** Distribution of earthquakes (black stars), stations (white triangles), and Rayleigh-wave ray-paths at periods  $T = 8$ – $40$  s. Four ray-path clusters are indicated by different colors. Cluster 1 (red) contains the rays from northwestern directions. Cluster 2 (green) includes the rays from north-northeast. Cluster 3 (cyan) consists of the rays from the east. Cluster 4 (violet) comprises the rays from south-southeast (e.g., Red Sea, Gulf of Aden and Arabian Sea).

## 2. Seismic data and Rayleigh-wave group-velocity measurements

The Saudi Geological Survey (SGS) has operated the permanent Saudi National Seismic Network (SNSN) since 2006, consisting of more than 300 stations (status December 2017). Most of the stations are equipped with either T40 or T120 Nanometrics sensors, while STS-2 Streckeisen instruments are operated at several sites. For our surface-wave investigation, we analyze vertical component seismograms from 77  $M_w \geq 5.5$  regional earthquakes with an epicentral distance  $\leq 30^\circ$ , recorded by the SNSN-stations in the years of 2007–2014. Rayleigh-wave group-velocity dispersion curves are measured by applying the multiple-filter technique (MFT) of Dziewonski et al. (1969; implemented in the Computer Programs in Seismology package of Herrmann and Ammon, 2002). The MFT analyzes signal amplitude as a function of velocity and period, applying a Gaussian filter to isolate the wave package of interest. The width of the Gaussian filter is chosen based on the epicentral distance to minimize the area of the fundamental mode

in the velocity-period profile surface (Ammon, 2001). Before applying the MFT approach, we remove the instrumental response to obtain seismograms of ground displacement.

We use over 3,000 seismograms to determine Rayleigh-wave group-velocities for periods  $T$  in the range  $8 \leq T \leq 40$  s. The lowest number of good quality measurements ( $\sim 1,100$  rays) has been obtained for  $T = 8$  s, due to the difficulty of measuring short-period group-velocities at large epicentral distances. The highest number of high quality group-velocity measurements ( $\sim 3,000$  rays) has been achieved for  $T = 20$  s. Fig. 2 displays the distribution of the regional earthquakes used, available SNSN-stations and corresponding Rayleigh-wave ray-paths (for periods  $T$  between 8 and 40 s) throughout Arabia. Seismic events are concentrated along plate boundaries, mainly the continental/oceanic rifts (e.g., Red Sea, Gulf of Aden, Indian Ocean Ridge) and the collision zones (e.g., Greece, Anatolia, Caucasus, Iran). In contrast, there are no earthquake within the Arabian Plate, except the M 5.7 event located in Harrat Lunayyir that is associated with the 2009 dike in-

trusion (Pallister et al., 2010). The spatial distribution, and hence coverage, of the 143 SNSN-stations is non-uniform, with high station density in western Saudi Arabia, in particular in the volcanic regions or in zones of recently increased seismic activity. Station spacing is much larger in the eastern Provinces. In general, the ray-path coverage is dense within the study area, however, the coverage varies with period, and hence the final spatial resolution of our inversion changes with period. Fig. S1 shows the corresponding ray-density maps.

To understand the spatial- and period-dependent resolution of our dataset, we group all ray-paths into four clusters according to the source location for each period (Fig. 2). The first cluster contains all ray-paths from northwestern directions. The second cluster includes the rays from Anatolia and Caucasus in the north-northeast. The third group consists of the ray-paths from the east, while the fourth group comprises the rays from the Red Sea, the Gulf of Aden and the Arabian Sea in southerly directions (Fig. 2). For each cluster, the distribution of group-velocity measurements follows a normal distribution (Fig. S2). To ensure that only high-quality measurements enter the subsequent inversion, we only retain group-velocity measurements that fall within three standard deviations (i.e., 99.7% of the dataset). Measurements beyond the three-sigma limits are discarded.

### 3. Rayleigh-wave group-velocity tomography

After measuring Rayleigh-wave group-velocities at various periods, we apply the Fast Marching Surface Tomography (FMST) scheme of Rawlinson (2005) to obtain Rayleigh-wave group-velocity maps. The FMST is implemented iteratively in two steps: first, the fast marching method (FMM) (Rawlinson and Sambridge, 2005) is applied for the forward prediction step, which is then followed by a subspace inversion scheme (Kennett et al., 1988) to invert for the depth-dependent S-wave structure. This last step includes the adjustment of the model parameters to satisfy the observed data. The FMM is a fast and stable grid-based numerical algorithm to compute the traveltimes field by solving the eikonal equation with finite-difference approximations (Rawlinson and Sambridge, 2005). The traveltimes from sources to receivers are calculated in 2-D spherical coordinates. The subspace inversion then projects the full linearized inverse problem into a much smaller  $n$ -dimensional model space, thus solving the inversion only for an  $n \times n$  matrix. The FMST is therefore an iterative nonlinear method, because the repeated operation of the FMM and the subspace inversion creates a nonlinear relationship between seismic wave velocity and traveltimes (Rawlinson and Sambridge, 2005).

The inversion scheme can be expressed as an optimization problem. The objective function is given by:

$$S(m) = (g(m) - d_{obs})C_d^{-1}(g(m) - d_{obs})^T + \varepsilon(m - m_0)C_m^{-1}(m - m_0)^T + \eta m D D^T m^T \quad (1)$$

where  $d_{obs}$  are the observed traveltimes,  $g(m)$  are the predicted traveltimes,  $m_0$  is the initial model,  $C_d^{-1}$  is an *a priori* data covariance matrix,  $C_m^{-1}$  is an *a priori* model covariance matrix,  $\varepsilon$  is the damping parameter,  $\eta$  is the smoothing factor, and  $D$  is the smoothness matrix. The first term on the right-hand side of Eq. (1) describes the search for a model  $m$  that minimizes the misfit between the predicted and observed data. The second term provides regularization to prevent the solution (e.g., final model) from straying too far from the initial model. The third term constrains the smoothness of the inverted model, limiting the spatial variations of model parameters between neighboring nodes.

We apply the FMST approach to the fundamental-mode Rayleigh-wave group-velocity measurements to obtain maps of group-velocity variations at periods of 8–40 s. The study region is pa-

rameterized as a 2-D rectangular grid with a node spacing of  $0.8^\circ$  in both latitude and longitude. We use the average group-velocities as initial values for tomographic inversion at each period. To choose the optimal damping and smoothing parameters, we investigate the trade-off curves between root-mean-square (RMS) and model variance, as well as between RMS and model roughness obtained at periods of 10 and 30 s (Fig. S3; damping varying between 0.2 and 5; smoothing parameter between 1 and 50). The optimal damping equals to 1, while the best smoothing parameter is 4. These values provide a good balance between model resolution and model roughness/variance. We also find that six iterations are usually sufficient to achieve convergence for the tomographic inversion.

Fig. 3 shows maps of Rayleigh-wave group-velocity variations relative to the average group-velocities at periods of 8, 10, 15, 20, 25, 30, and 40 s. For reference, we also plot the characteristic shear-velocity sensitivity kernels for Rayleigh-waves at different periods. At short periods (8–10 s) (Fig. 3a, b), group-velocity variations correlate well with surface geology. The low-velocity anomalies are located in the eastern and northern Arabia, delineating the main sedimentary units including the Arabian Platform, the Persian Gulf and the Mesopotamian Foredeep. Regions with thick sediments usually show much slower surface-wave group-velocities, since sedimentary rocks have lower shear-wave velocities than crystalline crustal rocks. At periods of 15–20 s (Fig. 3c, d), the correlation between the slow group-velocities and the sedimentary basins still persists. In addition, a remarkable high velocity anomaly beneath the southern Red Sea appears at 15 s period and disappears again at period of 40 s, indicating the possible presence of oceanic crust in the southern Red Sea. Since oceanic crust is generally thinner than continental crust, the mid-period Rayleigh-waves ( $T = 15$ –20 s, sensitive to 10–30 km depths) may be detecting the upper-mantle in this region. However, we note that these features are at the edge of good ray coverage domain, and hence are not well resolved.

In addition, we detect indications of locally reduced velocity (i.e., the faint regions of  $dU < 0$  km/s) below the Cenozoic volcanic fields at periods of 15–20 s. At longer periods ( $T = 25$ –40 s; Fig. 3e–g), low group-velocities are found which are likely due to the thicker continental crust under the Arabian Platform and the orogenic regions such as the Zagros Mountains. The surface-wave speed at intermediate periods ( $T = 25$ –40 s) is usually slower in the regions with thick crust, because crustal shear-velocities are much lower than upper-mantle shear-velocities.

To examine the spatial resolution of the tomographic inversion, given the available dataset, we conduct a series of checkerboard tests. Such tests are needed to understand the robustness and reliability of the inversion, and to assess in which region and for which period geophysical interpretations are possible. Typically, the bordering zones of the study are less well resolved due to fewer crossing rays, while the central part is characterized by denser ray coverage (Fig. S1). However, to gain insight what exactly can be resolved in such a study, checkerboard tests with changing grid spacing are conducted. Here, we construct for each period an initial test model by imposing a  $2.5^\circ \times 2.5^\circ$  checkerboard pattern comprising anomalies of  $\pm 0.8$  km/s group-velocity variations on a constant velocity background model (i.e., the corresponding average group-velocity), using a bi-cubic B-spline interpolation between grid-nodes. Synthetic traveltimes for the checkerboard model are computed using the FMM procedure with the same ray-paths of the observed data. Finally, we obtain the recovered velocity pattern using the node spacing desired in the final inversion ( $0.8^\circ \times 0.8^\circ$ ), applying also the same regularizations. We find that the checkerboard patterns are generally well recovered (Fig. S4) for periods of 10–30 s, but recovery of the checkerboard model at periods of 8 and 40 s is less convincing due to the lim-

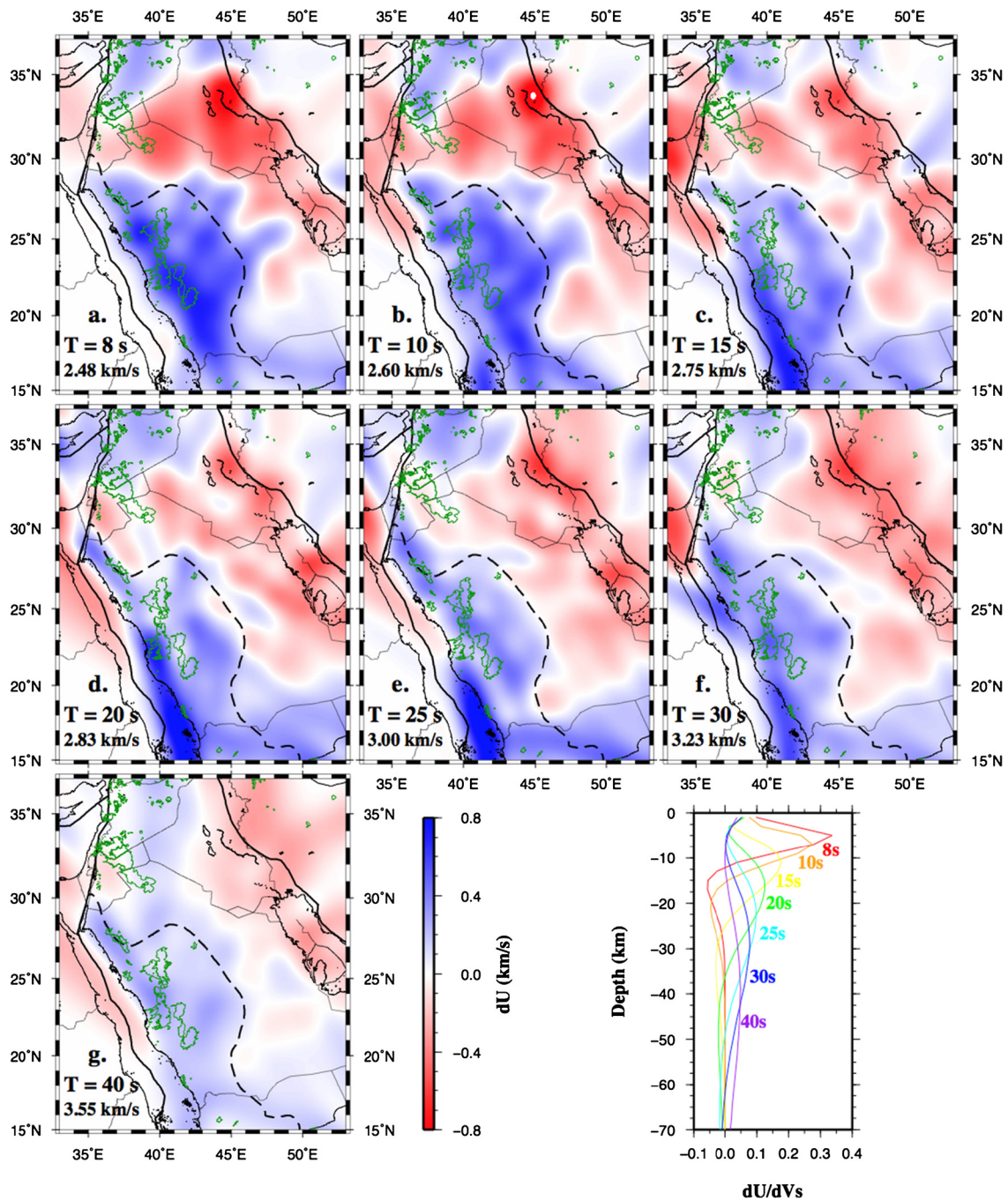


**Fig. 3.** Maps of Rayleigh-wave group-velocities (periods  $T = 8$ – $40$  s), showing perturbations relative to the corresponding average group-velocities (stated in each panel). Green contours outline the Cenozoic volcanism (Fig. 1). Dashed black line marks the boundary between the Arabian Shield and the Arabian Platform. For reference, we also plot the shear-wave sensitivity kernels of the Rayleigh-wave group-velocities at several periods.

ited ray coverage at these two periods (Fig. 2). We also remark that the periphery of our model domain is poorly resolved; correspondingly we only consider an irregularly shaped central region for later interpretation. Further checkerboard tests, trying lower group-velocity anomalies (e.g.,  $\pm 0.4$  km/s) and/or focusing on the local region of the Cenozoic volcanism, are included in the supplementary document (Figs. S5, S6).

#### 4. Shear-wave velocity inversion

Next, we invert the Rayleigh-wave group-velocities to obtain a 1-D shear-wave velocity-depth profile at each grid node, following the approach of Herrmann and Ammon (2002). These profiles

are then combined to generate a 3-D shear-velocity model of the Earth crust and upper-mantle below Saudi Arabia. Group-velocities between period 8 and 40 s are extracted from our tomography results, while we rely on group-velocity measurements of Ma and Masters (2014) at longer periods ( $T = 40$ – $133$  s) to constrain the lithospheric mantle. Ma and Masters (2014) obtained millions of high-quality fundamental-mode Rayleigh- and Love-wave group-velocity measurements at periods  $T = 25$ – $133$  s (utilizing a cluster analysis technique), and reported the global lateral variations of group-velocity. Their cluster approach measures surface-wave velocities for all recordings from a single event at a single target period, instead of making measurements for all periods for a single event-station pair (Ma and Masters, 2014). Although their tomo-

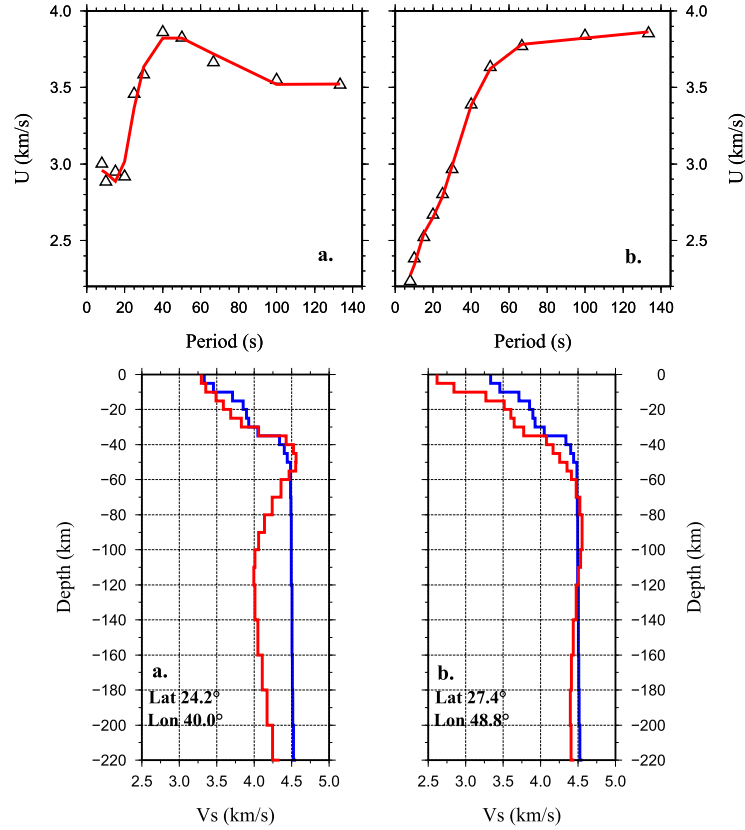


**Fig. 4.** Examples of the 1-D shear-velocity inversion at two nodes – (a) 24.2°N, 40.0°E on the Arabian Shield; (b) 27.4°N, 48.8°E on the Arabian Platform. The top panels show observed dispersion data (triangles) extracted from our tomography results (periods  $T = 8\text{--}40$  s) and from Ma and Masters (2014) (periods  $T = 40\text{--}133$  s), as well as the predicted dispersion curves (red). The bottom panels display the starting models (blue) and the inverted 1D shear-wave velocity models (red) at each location.

graphic results are based on a block size of  $1^\circ$  by  $1^\circ$ , the best resolution is around  $5^\circ$  (50 s period Rayleigh-wave, according to their checkerboard tests). Despite the nominal lower resolution of the Ma and Masters dataset, we consider it important for our study in order to help constrain the deeper (below  $\sim 50$  km depth) Earth structure underneath Saudi Arabia.

We parameterize our starting model as a stack of layers with constant thickness and constant velocity. Layer thicknesses are 5 km in the Earth crust and uppermost mantle (0–60 km), and then progressively increase to 10 km in the lithospheric mantle levels (60–120 km) and to 20 km at deeper depths. In our previous study (Tang et al., 2016), we constructed 1-D shear-wave velocity-depth profiles of crust and uppermost mantle at 56 SNSN-stations by jointly inverting P-wave receiver functions and surface-wave dispersion data. Correspondingly, we use the average shear-velocity model from these 56 SNSN-stations as the starting model for the depth range of 0–50 km, with P-velocity and density for each layer being based on the joint inversion models of Tang et al. (2016). At larger depths (50–220 km), we choose the global 1-D model AK135 as starting model. For the 1-D shear-velocity inversion at each grid node, differential smoothing is applied to damp the differences between the shear-wave velocity perturbations in adjacent layers (Herrmann and Ammon, 2002). The function to be minimized in the inversion can be expressed as  $\text{MIN} = |\delta y - \mathbf{A} \cdot \delta x| + |\theta \mathbf{D} \cdot \delta x|$ , where vector  $\delta x$  represents shear-velocity model perturbations,  $\delta y$  is the data residual, matrix  $\mathbf{A}$  contains the sensitivity kernel, vector  $\mathbf{D} \cdot \delta x$  contains the first differences between shear-velocity perturbations in adjacent layers, and  $\theta$  is the damping factor that we set equal to 1.

Fig. 4 illustrates the 1-D shear-velocity inversion procedure at two nodes. One node (Fig. 4a) is located on the Arabian Shield (lat. 24.2°, long. 40.0°), showing a  $\sim 35$  km thick crust, a very

thin upper-mantle lid, and slow velocities in the upper-mantle. In contrast, the other site (Fig. 4b) is on the Arabian Platform (lat. 27.4°, long. 48.8°), displaying thick sediments ( $\sim 10$  km), crust and lithosphere. Note that the observed Rayleigh-wave group-velocity dispersion curve (triangles in Fig. 4) is a combination of group-velocities at 8–40 s periods from our tomography, as well as the group-velocities at periods of 40–133 s from Ma and Masters (2014) within our study region. The starting model is a combination of the average 1-D model for 0–50 km depths from Tang et al. (2016), and the AK135 model for 50–220 km depths. Additionally, A few further tests and comparisons, such as applying a different starting model (e.g., AK135 model), comparing with the previous results from joint inversion (Tang et al., 2016), are included in the e-supplement (Figs. S7–S10).

To assess the spatial resolution of our 3-D model, we perform checkerboard tests with various grid parameterizations. The initial test model of variable input S-wave velocities follows a  $2.5^\circ \times 2.5^\circ$  checkerboard pattern with  $\pm 0.4$  km/s (i.e.,  $\pm 10\%$ ) S-wave anomalies in horizontal sections. In vertical direction, the signs change at depths of 5 km, 20 km, 40 km, and 70 km. The first step when creating the synthetic data is to compute 2-D maps of Rayleigh-wave group-velocities for all periods (i.e., 8–40 s). For each grid node within the study area, we then calculate expected group-velocities based on the 1-D model corresponding to that node. Subsequently, we compute the synthetic Rayleigh-wave travel times and apparent group-velocities for all included ray-paths (i.e., event – station pairs) in the original dataset at each period. We then treat the synthetic Rayleigh-wave travel times and apparent group-velocities as “real” data that we then use to perform the surface wave tomography. From the corresponding 2-D maps of group-velocities, we then invert for the shear-velocity model, following the same procedures described in sections 3 and 4. Fig. 5 shows the result of

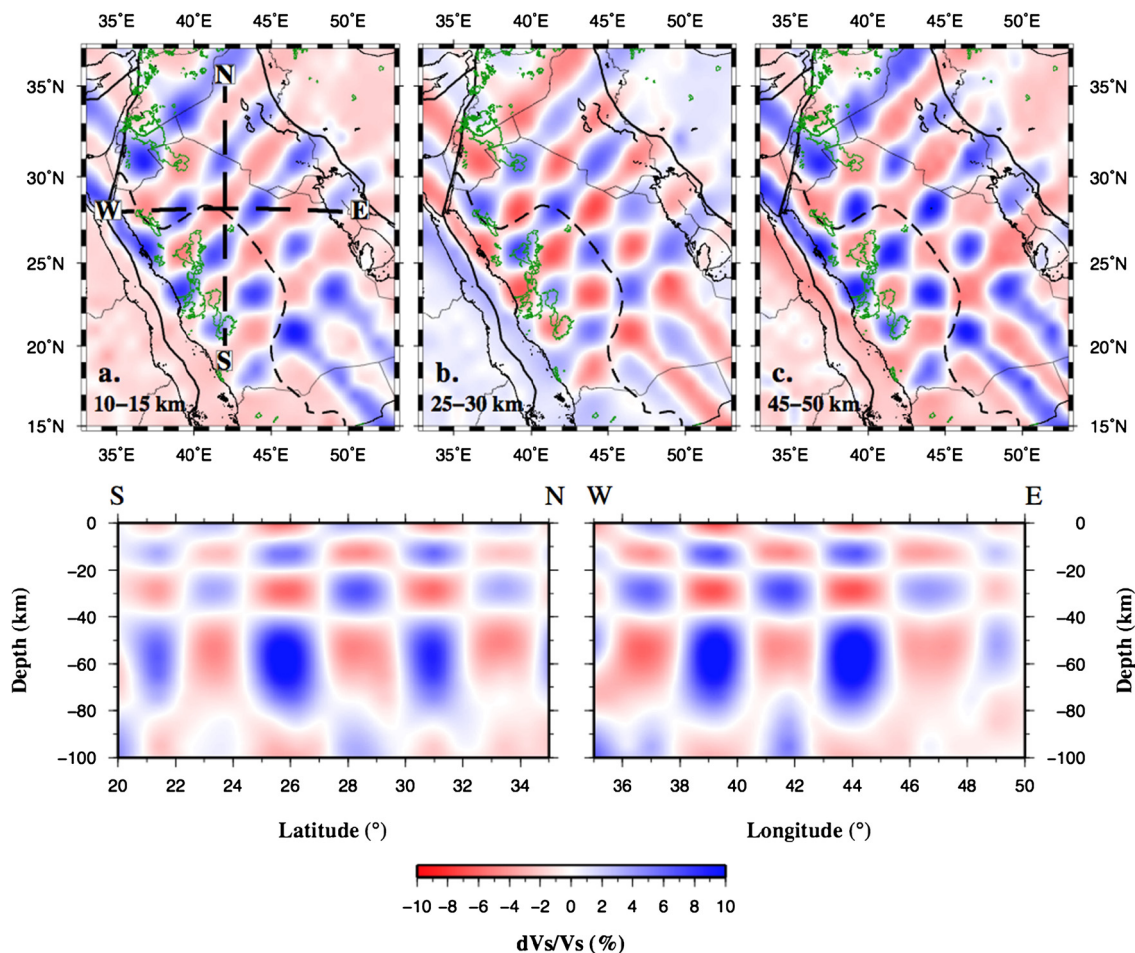


**Fig. 5.** Resolution tests for our study region, applying a  $2.5^\circ \times 2.5^\circ$  initial checkerboard pattern with imposed anomalies of  $\pm 0.4$  km/s (i.e.,  $\pm 10\%$ ). The top row displays the recovered shear-wave velocity patterns (at three different depths), indicating excellent resolution for the region of interest of the Cenozoic volcanic fields (marked by green lines). The bottom row presents the recovered depth-dependent velocity structure in two vertical cross-sections (locations in top-left panel).

the synthetic test for the entire study region. The three horizontal slices show that the checkerboard anomalies are well recovered in the central part of our study domain, but resolution degrades at the boundaries. In the southwest, this boundary roughly coincides with the Red Sea coastline. In the vertical sections, four layers with different signs of anomalies are well restored, indicating excellent resolution within the upper  $\sim 80$  km depth. These tests show the robustness of our inversion results, and provide important information for further geophysical, geological, geodynamic interpretation.

Finally, we obtain a set of 1-D inverted models that we interpolate to construct a 3-D shear-wave velocity model for Saudi Arabia. Fig. 6 displays a set of horizontal depth-slices of shear-wave velocity perturbations (in %) from our 3-D shear-wave velocity model at crustal levels. At 0–10 km depths (Fig. 6a, b), the S-wave velocity patterns clearly reflect our Rayleigh-wave group-velocity patterns at 8–10 s periods (Fig. 3a, b), in which slower velocities correlate well with the presence of sedimentary basins, including the Arabian Platform, the Persian Gulf and the Mesopotamian Foredeep. We also detect low velocity zones beneath the Cenozoic volcanic regions (i.e., harrats) at 10–30 km depths (Fig. 6c–f), with S-wave velocity reductions of 2–3% with respect to the corresponding reference wave speeds. Even at 25–30 km depths (Fig. 6f), most areas, including the Platform and the eastern Shield, show crustal shear-velocities that are comparatively slow, while the Red Sea margin indicates relatively high velocities corresponding to S-wave speeds expected at the lower-crustal levels and near the Moho. In summary, we detect thinner crust along the Arabian margin of the

Red Sea, which has been hinted in previous studies (Al-Damegh et al., 2005; Tkalčić et al., 2006; Tang et al., 2016). At 30–35 km depths (Fig. 6g), most regions of the Arabian Shield have reached the lower crust and even Moho discontinuity. However, both the southern Arabian Shield and the Arabian Platform are still showing crustal velocities ( $\sim 3.7$ – $3.9$  km/s). At 35–45 km depths (Fig. 6h, i), we find that S-wave speeds underneath the Arabian Shield has reached values expected at the Moho and the uppermost mantle. In contrast, the southern Arabian Shield and the Arabian Platform reveal still lower-crustal velocities. Our high-resolution study therefore clearly demonstrates that the southern Arabian Shield and the Arabian Platform have thicker crust ( $\geq 45$  km) than the western part of the Arabian Shield ( $\sim 35$ – $40$  km), corroborating previous results (Tang et al., 2016).

Fig. 7 displays horizontal depth-slices of S-wave velocity anomalies for upper-mantle depth levels. We find a substantial low S-wave velocity anomaly underneath the southwestern part of our study region, near the Red Sea coastline (Fig. 7b–l), continuing from  $\sim 50$  km to perhaps over 180 km depths. This may be related to findings by Chang and Van der Lee (2011). They mapped slow S-wave velocities within the upper-mantle below the southern Red Sea. This domain of low S-wave velocities implies that the lithospheric thickness is no more than 50 km beneath the southern Red Sea and the nearby coastal regions, consistent with previous local LAB estimations (Hansen et al., 2007).

In addition, we identify isolated low S-wave velocity anomalies beneath the areas of Cenozoic volcanism in the Arabian Shield, extending over the depth range 55–70 km (Fig. 7c, d). As depth in-

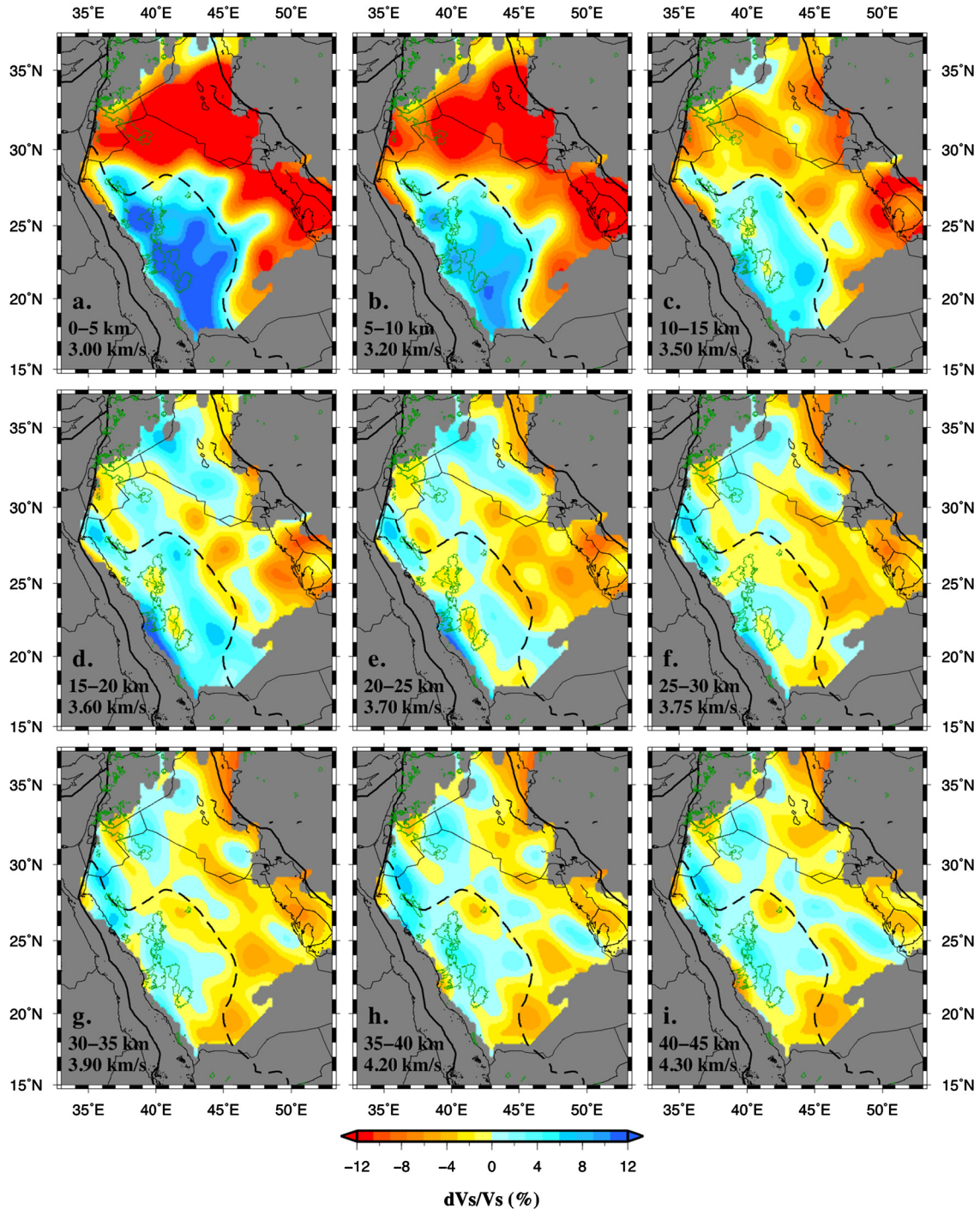


**Fig. 6.** Horizontal slices of shear-velocity anomalies (in percentage deviation from the reference velocities) over the crustal depth range of the Arabian Plate (0–45 km). The reference velocity values and depths are indicated in the bottom-left corners of each panel. Green contours outline the regions of Cenozoic volcanism. Dashed black line marks the boundary between the Arabian Shield and the Arabian Platform. Note that we only show shear-wave variations over the region which we consider well resolved based on the ray-density maps (Fig. S1) and the checkerboard resolution tests (Figs. 5, S4, S5).

creases, these low velocity anomalies expand into interconnected low shear-velocity zones (LVZ), including the Arabian Shield and even northern Arabia (beneath Jordan and Syria, however, the resolution of our model is limited in this region). Our results thus corroborate and extend previous findings regarding the LVZ that have been proposed, being a northward extension from the Afar plume (Chang and Van der Lee, 2011; Chang et al., 2011; Yao et al., 2017). Our velocity maps also indicate thin lithosphere (~60–90 km thick) and slower upper-mantle S-wave velocities in the Arabian Shield, compared to thicker lithosphere and relatively

high upper-mantle velocities of the Arabian Platform. However, our 3-D inversion model cannot reveal further details of this LVZ, because the upper-mantle structure is largely constrained by the large-scale group-velocity tomography of Ma and Masters (2014) whose resolution is spatially limited.

## 5. Discussion and implications

The most intriguing features in our 3-D model are the zones of low S-wave velocity at crustal levels underneath the regions

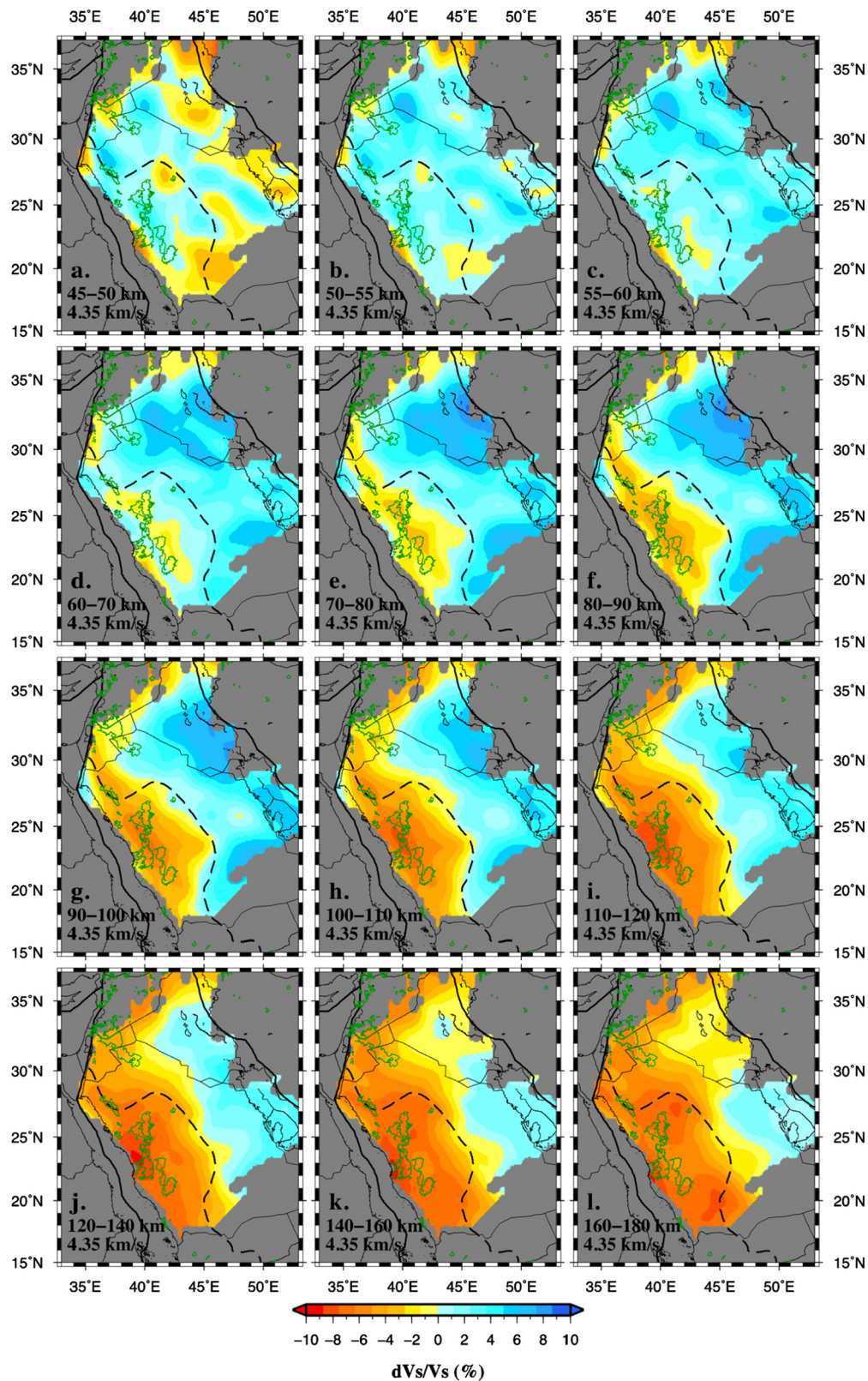
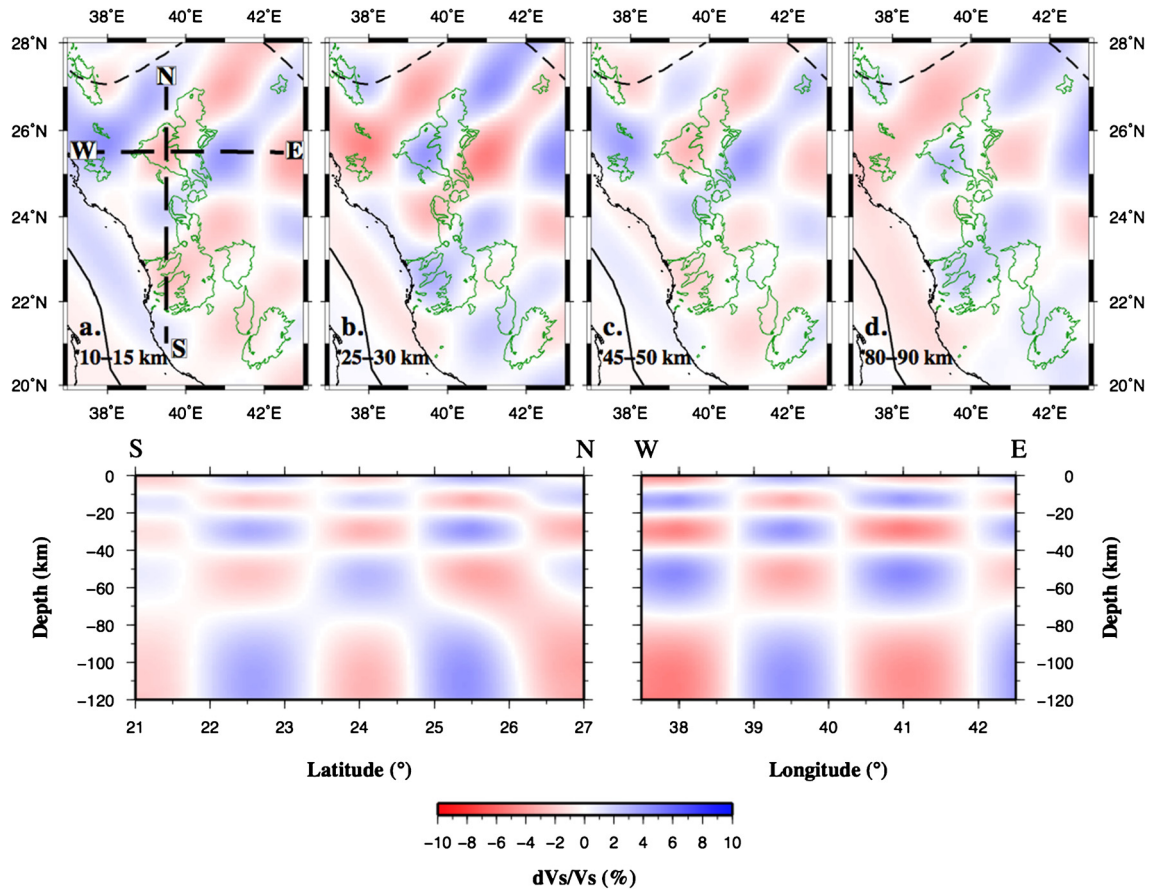


Fig. 7. Same as Fig. 6, but for the upper-mantle level (45–180 km) beneath Saudi Arabia. Here, a common reference shear-wave velocity of 4.35 km/s is applied.

of Cenozoic volcanism, and the upper-mantle LVZ below the Arabian Shield. In the following, we discuss possible explanations for the presence of these S-wave velocity anomalies as well as implications for understanding the Cenozoic volcanism of western Arabia.

### 5.1. S-wave anomalies underneath the Cenozoic volcanism

Our inversion documents the presence of low S-wave velocity anomalies at 10–30 km depths below the Cenozoic volcanic areas (Fig. 6c–f) of Saudi Arabia. To further examine the details of



**Fig. 8.** Resolution tests focusing on the regions of Cenozoic volcanism in the western Arabian Shield. A  $1.5^\circ \times 1.5^\circ$  checkerboard pattern with imposed S-velocity anomalies of  $\pm 0.4$  km/s (i.e.,  $\pm 10\%$ ), also varying with depths, is applied as initial test model. See Fig. 5 for further details. Note that the recovered model indicates adequate resolution over the volcanic areas, while resolution rapidly degrades near the Red Sea.

these low-velocity features, we zoom into the regions of Cenozoic volcanism in the Arabian Shield to obtain images of higher spatial resolution. For this purpose, we follow the same procedure as before, conducting Rayleigh-wave group-velocity tomography followed by shear-wave velocity inversion with all available rays and stations, but now focusing on the local harrats. Because the spacing of the SNSN-stations is much denser over the region of Cenozoic volcanism, hence better ray coverage is achieved that allows a closer node spacing of  $0.5^\circ$  in both latitude and longitude (instead of  $0.8^\circ$  as previously). Furthermore, we experiment with the needed regularizations for the Rayleigh-wave tomography, and find optimal smoothing ( $\eta = 2$ ) and damping parameter ( $\varepsilon = 1$ ) for obtaining higher resolution velocity maps. As a result, we are able to generate a refined 3-D shear-wave velocity model for the area of Cenozoic volcanism. As before, we carry out checkerboard tests for this local region (Fig. 8) to assess the robustness and reliability of our inversion. The horizontal resolution for the local 3-D model is about  $1.5^\circ \times 1.5^\circ$ , which is substantially better than that for the entire study area. Correspondingly, the depth-dependent velocity anomalies under the volcanic areas are well resolved (Fig. 8).

We present our findings in terms of deviations of local S-wave speed in nine horizontal slices (Fig. 9) and three vertical sections (Fig. 10). The local 3-D model reveals low shear-wave velocity anomalies beneath the Cenozoic volcanic fields at crustal levels. These include the low velocity zone at  $\sim 10$ – $25$  km depths near Harrat Rahat and Harrat Khaybar, the low velocities at  $\sim 10$ – $35$  km depths extending from Harrat Khaybar, to Harrat Lunayyir and Harrat Uwayrid, and the low velocity feature at  $\sim 10$ – $35$  km depths directly below Harrat Nawasif, Harrat Hadan and Harrat Kishb. The reduction in shear-wave speed appear largest in the later area,

reaching  $\sim 5\%$ , while overall it is on the order of 2–3% in lower-crustal depths (15–35 km). We also detect a low velocity anomaly at roughly 25–50 km depths in the northeastern corner of the study domain, perhaps related to Harrat Hutaymah. The vertical transects (Fig. 10) provide further details on the depth extent and lateral variations of the low velocity features below the harrats.

Interpreting in detail these regions of reduced shear-wave speed is not straightforward, as additional geophysical and geological information (temperature gradient, attenuation, anisotropy, conductivity, mineralogy) are missing in order to decipher the rock composition and potential presence of partial melts. Naturally, the zones of low S-wave speed underneath Cenozoic volcanic fields lend themselves to be interpreted as regions of partial melts that somehow feed the surface volcanism. However, let us first discuss the spatial pattern of the observed low S-wave velocities before we speculate about their nature.

Fig. 10 shows that the zone of low S-wave speed within the upper-mantle connects to the crustal low velocity zones in the region of Harrat Khaybar, northern Harrat Rahat, and Harrat Uwayrid. This suggests a possible “conduit” (between  $\sim 40$ – $70$  km depths, at lat.  $\sim 26^\circ$  and long.  $\sim 39.5^\circ$ ) through which magma may ascend from the upper mantle levels into the crust. This “conduit” appears to bifurcate into several branches (Fig. 10, cross-section C–C’). One branch ascends toward the southeast, arriving below Harrat Khaybar and northern Harrat Rahat. Another branch rises toward the northwest, reaching Harrat Uwayrid. The third one rises toward the west, arriving beneath Harrat Lunayyir, while another one appears to stretch towards the east at depths of around 20 km. Our findings therefore suggest the possible existence of a complex network of potential magma conduits that may

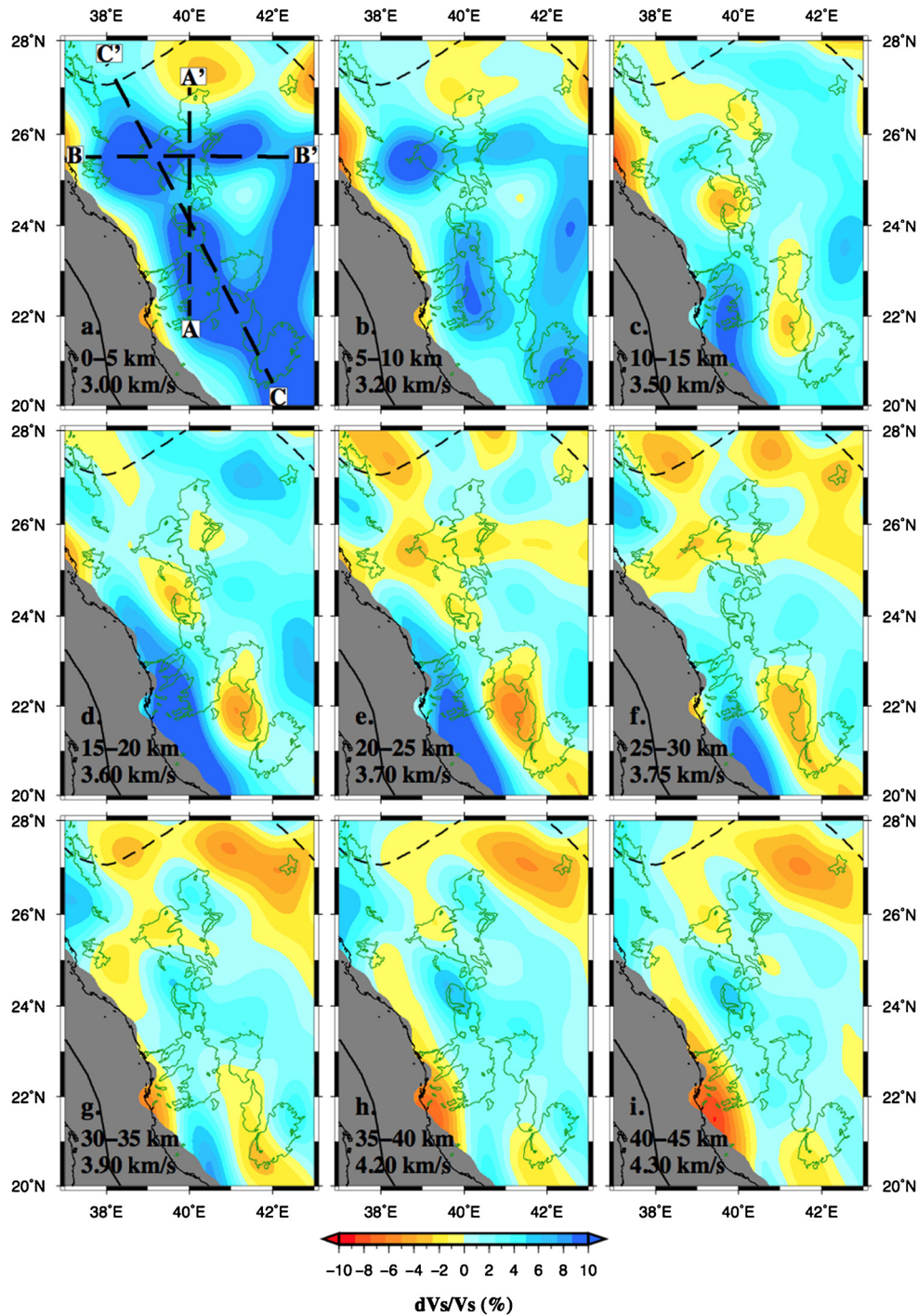


**Fig. 9.** Horizontal slices of shear-velocity anomalies at the crustal levels (0–45 km) below the Cenozoic volcanic regions, given in percentage deviation from the depth-dependent reference S-wave speeds (specified in the bottom-left of each panel). Green lines mark the volcanic areas. Dashed thick black lines in panel (a) indicate the three cross sections shown in Fig. 10.

feed the Cenozoic surface volcanism in Saudi Arabia. Notice also the regions of low S-wave speed beneath Harrat Nawasif, Harrat Hadan, and Harrat Kishb are disconnected from the upper-mantle LVZ, while the S-wave anomalies under Harrat Khaybar, northern Harrat Rahat, and Harrat Uwayrid are connected to the upper-mantle LVZ. It is interesting to note that the age of surface lavas in the harrats decreases from south to north (roughly coinciding with profile C–C' in Fig. 10) (Camp and Roobol, 1992), thus, the S-wave anomalies under the southern harrats (with older lavas) appear as currently isolated features in the crust. Further support for our results are provided by Koulakov et al. (2015) who map

lower S-velocities, higher P-velocities and increased  $V_p/V_s$  ratios at ~7–15 km depths under Harrat Lunayyir, which they interpret as a steady-state magma reservoir. They also suggest the presence of a conduit below ~15 km depth for fluids and melts from deeper sources.

## 5.2. Origin of Cenozoic volcanism

Fig. 10 reveals a spatial correlation of the S-wave anomalies with the Cenozoic surface volcanism, however, correlation does not mean causality. Yet, the inferred localized reductions in shear-

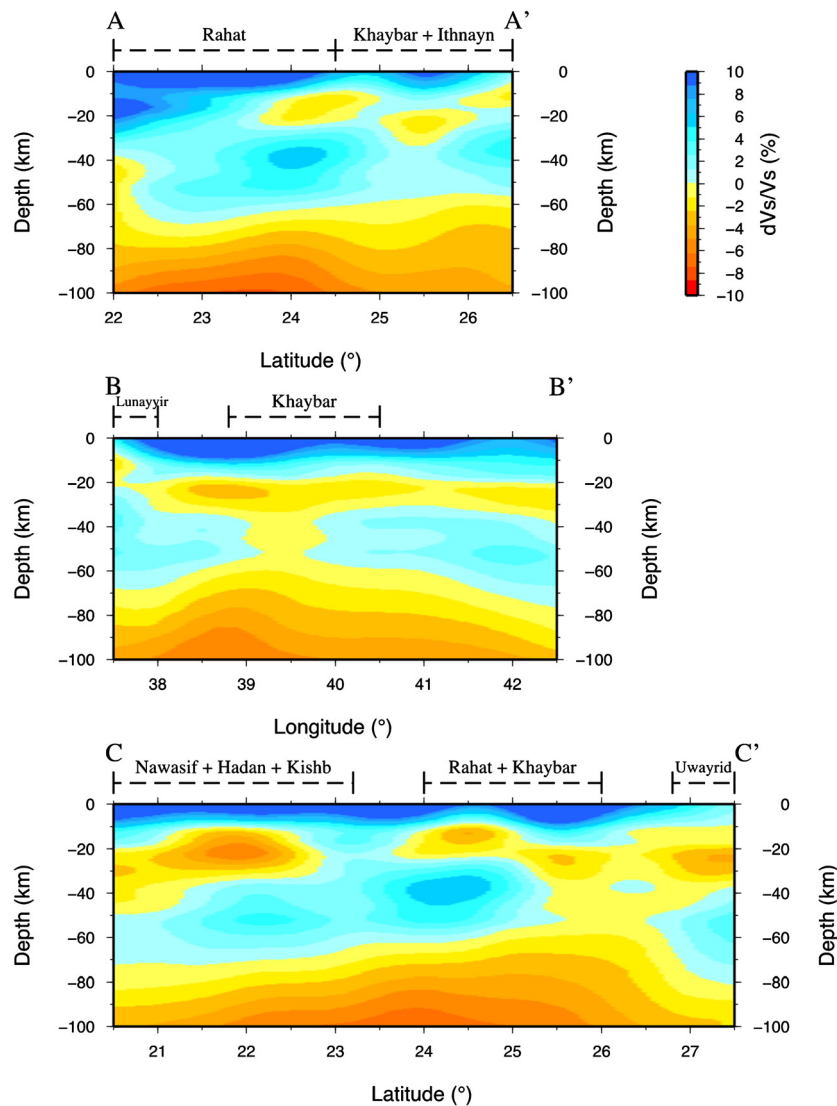


**Fig. 10.** Vertical profiles of shear-velocity anomalies (in percentage deviation) for the three transects shown in Fig. 9a. The reference velocities for each depth-range are indicated in Fig. 6 and 7.

wave speed of 2–3% (locally even 5%) that we observe underneath the harrats may be related to the origin of the volcanism. Since further geophysical information for these depths (15–35 km) in terms of conductivity, attenuation, or anisotropy are absent that are needed to determine the physical in-situ rock properties, we can only hypothesize what these velocity reductions represent. Following Hacker et al. (2014) and their approach on estimating the effect of melt on shear-wave speed based on Schmeling (1985), we find that 3% S-wave speed reductions can be explained by 1.5–3.5% partial melt, depending on melt geometry. For 2% S-wave velocity reduction, this percentage of partial melt reduces to 1.0–2.5%; for a –5% shear-wave-speed anomaly, 2.5–5.0% partial melt is expected. As we lack more detailed geological and geophysical information, we speculate that the imaged shear-wave velocity reductions of ~3% are due to ~2% partial melts that are localized in relatively broad anomalies of 50–100 km horizontal and 10–15 km vertical extent (Fig. 10). Notice that 2% of partial melt is considered a small amount, which however is sufficient to significantly reduce the S-wave speed (Hacker et al., 2014).

If indeed present, how are these small amount of partial melts generated? Our images of the upper-mantle LVZ across the Arabian Shield and even into Jordan may provide some clues. Associated with the approximately north–south orientation of the fast axis

from shear-wave splitting measurements (Gashawbeza et al., 2004; Hansen et al., 2006; Elsheikh et al., 2014), our results are consistent with the model of lateral mantle flow from the Afar hotspot (Chang and Van der Lee, 2011; Chang et al., 2011). However, the relation between the laterally-transported plume material and the surface volcanism in the western Arabia remains ambiguous. If large amounts of migrated Afar plume material is heating (even “flooding”) the bottom of the Arabian Shield’s lithosphere (Ebinger and Sleep, 1998; Chang and Van der Lee, 2011; Chang et al., 2011), local lithospheric melts and mixed plume material should feed the Cenozoic volcanism. However, geochemical analyses (Bertrand et al., 2003) on basalts report that the magmas for the volcanism in Saudi Arabia, Jordan and Syria do not originate from Afar mantle-plume material, but rather from Arabian lithospheric mantle. Also, the western Arabian lavas are not affected by crustal contamination (Bertrand et al., 2003), although some possible contaminants residing in both upper and lower crust have been identified in some basalts from Yemen (Baker et al., 1996, 1997). In addition, Konrad et al. (2016) reports that only lavas found at Harrat Rahat (directly above the MMN line) show a “weak but detectable plume signal”, suggesting only a small quantity of entrained plume material, whereas the dominant magma source for all the other harrats appears to be the Proterozoic lithospheric

mantle. Therefore, it seems likely that only a small amount of plume material from Afar has arrived at the southern tip (i.e., Harrat Rahat) of the MMN volcanic line. The typical mantle convection speed near the crust is  $\sim 20$  mm/yr (Liu et al., 2007). Assuming a similar velocity for the lateral northwards mantle flow from the Afar, the distance traveled for the laterally-transported Afar plume material is  $\sim 600$  km since the onset of Cenozoic volcanism (i.e.,  $\sim 30$  Ma). Obviously, this distance is insufficient to cover the Arabian Shield.

Correspondingly, the hypothesized fraction of partial melt is likely produced locally, at least to a large extent. Partial melting may occur in form of decompression melting, in the present case triggered by lithospheric thinning associated with the Red Sea rifting. Additional heating due to lateral mantle flow from the Afar hotspot may further contribute to the lithospheric melting under the southern Arabian Shield.

However, to map further details of the inferred low shear-wave speed anomalies and to understand their rock-physical properties and geodynamic origin, further geophysical investigations, associated with geochemical and geological studies, are needed. These will also help to address the question whether there is a lithospheric-to-crustal “plumbing system” underneath the Arabian Shield that feeds the Cenozoic volcanism, or whether the well-resolved low shear-velocity anomalies present deep-seated isolated reservoirs of partial melts that are occasionally fed by lithospheric melts mixed with local asthenospheric mantle material.

## 6. Conclusions

We conduct a fundamental-mode Rayleigh-wave group-velocity tomography and develop a 3-D shear-velocity model of the crust and upper-mantle for Saudi Arabia and its adjacent regions using the regional seismic data. Through a series of checkerboard tests, we establish the limits of resolution of our dataset, and thus document good spatial resolution over most parts of the study region. Our results greatly improve previous models of crust-and-mantle structure underneath Saudi Arabia, and help investigating the underlying geodynamical processes in this area. In particular, we identify low shear-wave velocity anomalies at crustal levels in regions of Cenozoic surface volcanism, which we interpret as areas that comprise  $\sim 2\%$  partial melt. We also image the upper-mantle LVZ below the western Arabia, supporting a previous model of lateral mantle migration from the Afar hotspot (Chang et al., 2011). We speculate that only a small amount of plume material from the Afar has arrived at the southern tip (i.e., Harrat Rahat) of the Cenozoic volcanism area. The generation of local lithospheric mantle melts under the Arabian Shield may be caused by decompression partial melting associated with lithospheric thinning during the Red Sea opening. In this case, lithospheric melts, mixed with local asthenospheric material, may provide the main magma source of the late-Cenozoic volcanism in the western Arabia.

## Acknowledgements

We thank Dr. Mahmoud Salam, Wael Raddidi, and the entire team at the National Center for Earthquakes and Volcanoes (NCEV) at the Saudi Geological Survey (SGS) for providing the broadband seismic data. We also thank Mohammed Soliman and two anonymous reviewers for their constructive comments that help greatly to improve the manuscript. We acknowledge support by Kangwon National University (KNU) for hosting Z.T. during a research collaboration visit in September 2015. The research presented in this paper was supported by funding from King Abdulah University of Science and Technology (KAUST), grant number BAS/1/1339-01-01. S.-J.C. was supported by the Korea Meteorological

Administration Research and Development Program under grant KMIPA 2015-7030.

## Appendix A. Supplementary material

Supplementary material related to this article can be found online at <https://doi.org/10.1016/j.epsl.2018.05.011>.

## References

- Al-Damegh, K., Sandvol, E., Barazangi, M., 2005. Crustal structure of the Arabian plate: new constraints from the analysis of teleseismic receiver functions. *Earth Planet. Sci. Lett.* 231 (3), 177–196.
- Ammon, C.J., 2001. Notes on Seismic Surface-Wave Processing, Part I, Group Velocity Estimation. Saint Louis University. Version 3(0).
- Baker, J.A., Thirlwall, M.F., Menzies, M.A., 1996. Sr–Nd–Pb isotopic and trace element evidence for crustal contamination of plume-derived flood basalts: Oligocene flood volcanism in western Yemen. *Geochim. Cosmochim. Acta* 60 (14), 2559–2581.
- Baker, J.A., Menzies, M.A., Thirlwall, M.F., Macpherson, C.G., 1997. Petrogenesis of Quaternary intraplate volcanism, Sana'a, Yemen: implications for plume–lithosphere interaction and polybaric melt hybridization. *J. Petrol.* 38 (10), 1359–1390.
- Bellahsen, N., Faccenna, C., Funicello, F., Daniel, J.M., Jolivet, L., 2003. Why did Arabia separate from Africa? Insights from 3-D laboratory experiments. *Earth Planet. Sci. Lett.* 216 (3), 365–381.
- Bertrand, H., Chazot, G., Blichert-Toft, J., Thorai, S., 2003. Implications of widespread high- $\mu$  volcanism on the Arabian Plate for Afar mantle plume and lithosphere composition. *Chem. Geol.* 198 (1), 47–61.
- Bosworth, W., Huchon, P., McClay, K., 2005. The Red Sea and Gulf of Aden basins. *J. Afr. Earth Sci.* 43 (1), 334–378.
- Brown, G.F., 1972. Tectonic Map of the Arabian Peninsula. No. 72-52. US Geological Survey.
- Camp, V.E., Roobol, M.J., 1992. Upwelling asthenosphere beneath western Arabia and its regional implications. *J. Geophys. Res.* 97 (B11), 15255–15271.
- Chang, S.J., Merino, M., Van der Lee, S., Stein, S., Stein, C.A., 2011. Mantle flow beneath Arabia offset from the opening Red Sea. *Geophys. Res. Lett.* 38 (4).
- Chang, S.J., Van der Lee, S., 2011. Mantle plumes and associated flow beneath Arabia and East Africa. *Earth Planet. Sci. Lett.* 302 (3), 448–454.
- Cochran, J.R., Martinez, F., 1988. Evidence from the northern Red Sea on the transition from continental to oceanic rifting. *Tectonophysics* 153 (1–4), 25–53.
- Daradich, A., Mitrovica, J.X., Pysklywec, R.N., Willett, S.D., Forte, A.M., 2003. Mantle flow, dynamic topography, and rift-flank uplift of Arabia. *Geology* 31 (10), 901–904.
- Dziewonski, A., Bloch, S., Landisman, M., 1969. A technique for the analysis of transient seismic signals. *Bull. Seismol. Soc. Am.* 59 (1), 427–444.
- Ebinger, C.J., Sleep, N.H., 1998. Cenozoic magmatism throughout East Africa resulting from impact of a single plume. *Nature* 395 (6704), 788–791.
- Elsheikh, A.A., Gao, S.S., Liu, K.H., Mohamed, A.A., Yu, Y., Fat-Helbary, R.E., 2014. Seismic anisotropy and subduction-induced mantle fabrics beneath the Arabian and Nubian Plates adjacent to the Red Sea. *Geophys. Res. Lett.* 41 (7), 2376–2381.
- Garfunkel, Z., Beyth, M., 2006. Constraints on the structural development of Afar imposed by the kinematics of the major surrounding plates. *Geol. Soc. (Lond.) Spec. Publ.* 259 (1), 23–42.
- Gashawbeza, E.M., Klempner, S.L., Nyblade, A.A., Walker, K.T., Keranen, K.M., 2004. Shear-wave splitting in Ethiopia: Precambrian mantle anisotropy locally modified by Neogene rifting. *Geophys. Res. Lett.* 31 (18).
- Gettings, M.E., Blank, H.R., Mooney, W.D., Healey, J.H., 1986. Crustal structure of southwestern Saudi Arabia. *J. Geophys. Res., Solid Earth* (1978–2012) 91 (B6), 6491–6512.
- Hacker, B.R., Ritzwoller, M.H., Xie, J., 2014. Partially melted, micabearing crust in Central Tibet. *Tectonics* 33, 1408–1424. <https://doi.org/10.1002/2014TC003545>.
- Hansen, S.E., Rodgers, A.J., Schwartz, S.Y., Al-Amri, A.M., 2007. Imaging ruptured lithosphere beneath the Red Sea and Arabian Peninsula. *Earth Planet. Sci. Lett.* 259 (3), 256–265.
- Hansen, S., Schwartz, S., Al-Amri, A., Rodgers, A., 2006. Combined plate motion and density-driven flow in the asthenosphere beneath Saudi Arabia: evidence from shear-wave splitting and seismic anisotropy. *Geology* 34 (10), 869–872.
- Herrmann, R., Ammon, C., 2002. Computer Programs in Seismology, Version 3.30. Saint Louis University, St. Louis, Missouri.
- Julià, J., Ammon, C.J., Herrmann, R.B., 2003. Lithospheric structure of the Arabian Shield from the joint inversion of receiver functions and surface-wave group velocities. *Tectonophysics* 371 (1), 1–21.
- Kaban, M.K., El Khrepy, S., Al-Arif, N., Tesauro, M., Stolk, W., 2016. Three-dimensional density model of the upper mantle in the Middle East: interaction of diverse tectonic processes. *J. Geophys. Res., Solid Earth* 121 (7), 5349–5364.
- Kennett, B.L.N., Sambridge, M.S., Williamson, P.R., 1988. Subspace methods for large inverse problems with multiple parameter classes. *Geophys. J. Int.* 94 (2), 237–247.

- Konrad, K., Graham, D.W., Thornber, C.R., Duncan, R.A., Kent, A.J., Al-Amri, A.M., 2016. Asthenosphere–lithosphere interactions in Western Saudi Arabia: inferences from  $^3\text{He}/^4\text{He}$  in xenoliths and lava flows from Harrat Hutaymah. *Lithos* 248, 339–352.
- Koulakov, I., Burov, E., Cloetingh, S., El Khrepy, S., Al-Arifi, N., Bushenkova, N., 2016. Evidence for anomalous mantle upwelling beneath the Arabian Platform from travel time tomography inversion. *Tectonophysics* 667, 176–188.
- Koulakov, I., El Khrepy, S., Al-Arifi, N., Kuznetsov, P., Kasatkina, E., 2015. Structural cause of a missed eruption in the Harrat Lunayyir basaltic field (Saudi Arabia) in 2009. *Geology* 43 (5), 395–398.
- Kumar, M.R., Ramesh, D.S., Saul, J., Sarkar, D., Kind, R., 2002. Crustal structure and upper mantle stratigraphy of the Arabian shield. *Geophys. Res. Lett.* 29 (8), 130–131.
- Liu, J., Liu, Q.Y., Guo, B., Yuen, D.A., Song, H.Z., 2007. Small-scale convection in the upper mantle beneath the Chinese Tian Shan Mountains. *Phys. Earth Planet. Inter.* 163 (1), 179–190.
- Ma, Z., Masters, G., 2014. A new global Rayleigh- and Love-wave group velocity dataset for constraining lithosphere properties. *Bull. Seismol. Soc. Am.* 104 (4), 2007–2026.
- McGuire, A.V., Bohannon, R.G., 1989. Timing of mantle upwelling: evidence for a passive origin for the Red Sea rift. *J. Geophys. Res., Solid Earth* 94 (B2), 1677–1682.
- Mokhtar, T.A., Al-Saeed, M.M., 1994. Shear wave velocity structures of the Arabian Peninsula. *Tectonophysics* 230 (1), 105–125.
- Mokhtar, T.A., Ammon, C.J., Herrmann, R.B., Ghalib, H.A.A., 2001. Surface wave velocities across Arabia. *Pure Appl. Geophys.* 158 (8), 1425–1444.
- Mooney, W.D., Gettings, M.E., Blank, H.R., Healy, J.H., 1985. Saudi Arabian seismic-refraction profile: a traveltimes interpretation of crustal and upper mantle structure. *Tectonophysics* 111 (3), 173–246.
- Pallister, J.S., McCausland, W.A., Jónsson, S., Lu, Z., Zahran, H.M., El Hadidy, S., Moufti, M.R., et al., 2010. Broad accommodation of rift-related extension recorded by dyke intrusion in Saudi Arabia. *Nat. Geosci.* 3 (10), 705–712.
- Rawlinson, N., 2005. FMST: Fast Marching Surface Tomography Package – Instructions. Research School of Earth Sciences, Australian National University, Canberra.
- Rawlinson, N., Sambridge, M., 2005. The fast marching method: an effective tool for tomographic imaging and tracking multiple phases in complex layered media. *Explor. Geophys.* 36 (4), 341–350.
- Rodgers, A.J., Walter, W.R., Mellors, R.J., Al-Amri, A.M., Zhang, Y.S., 1999. Lithospheric structure of the Arabian Shield and Platform from complete regional waveform modelling and surface wave group velocities. *Geophys. J. Int.* 138 (3), 871–878.
- Sandvol, E., Seber, D., Calvert, A., Barazangi, M., 1998. Grid search modeling of receiver functions: implications for crustal structure in the Middle East and North Africa. *J. Geophys. Res., Solid Earth (1978–2012)* 103 (B11), 26899–26917.
- Schmeling, H., 1985. Numerical models on the influence of partial melt on elastic, anelastic and electric properties of rocks, part I: elasticity and anelasticity. *Phys. Earth Planet. Inter.* 41, 34–57.
- Stoeser, D.B., Camp, V.E., 1985. Pan-African microplate accretion of the Arabian Shield. *Geol. Soc. Am. Bull.* 96 (7), 817–826.
- Tang, Z., Julià, J., Zahran, H., Mai, P.M., 2016. The lithospheric shear-wave velocity structure of Saudi Arabia: young volcanism in an old shield. *Tectonophysics* 680, 8–27.
- Tkalčić, H., Pasyanos, M.E., Rodgers, A.J., Gök, R., Walter, W.R., Al-Amri, A., 2006. A multistep approach for joint modeling of surface wave dispersion and teleseismic receiver functions: implications for lithospheric structure of the Arabian Peninsula. *J. Geophys. Res., Solid Earth (1978–2012)* 111 (B11).
- Wernicke, B., 1985. Uniform-sense normal simple shear of the continental lithosphere. *Can. J. Earth Sci.* 22 (1), 108–125.
- Xu, W., Jónsson, S., 2014. The 2007–2008 volcanic eruption on Jebel at Tair island (Red Sea) observed by satellite radar and optical images. *Bull. Volcanol.* 76 (2), 1–14.
- Yao, Z., Mooney, W.D., Zahran, H.M., Youssef, S.E.H., 2017. Upper mantle velocity structure beneath the Arabian Shield from Rayleigh surface wave tomography and its implications. *J. Geophys. Res., Solid Earth* 122 (8), 6552–6568.